

Bauschinger and size effects in thin-film plasticity

Y. Xiang, J.J. Vlassak *

Division of Engineering and Applied Sciences, Harvard University, 29 Oxford Street, Cambridge, MA 02138-2901, USA

Received 23 March 2006; received in revised form 27 June 2006; accepted 29 June 2006

Available online 2 October 2006

Abstract

We present an experimental investigation of the effects of surface passivation, film thickness and grain size on the plastic behavior of freestanding Cu thin films. The stress–strain curves of the films are measured using the plane–strain bulge test. Films with a passivation layer on one or both surfaces have an offset yield stress that increases significantly with decreasing film thickness; the yield stress of unpassivated films, by contrast, is relatively independent of film thickness and increases mainly as a result of grain-size strengthening. The stress–strain curves of passivated films show an unusual Bauschinger effect on unloading. This effect is not observed for unpassivated films. Our experimental results suggest that passivation layers prevent dislocations from exiting the films and that they block slip bands at the film–passivation interface. The back stresses associated with these blocked slip bands increase the resistance to forward plastic flow on loading and cause reverse plastic flow on unloading. The effect of the back stresses increases with decreasing film thickness and leads to the observed strengthening of the passivated films. The constraint of a passivating layer on dislocation motion and hence on plastic flow cannot be described by classical plasticity theories, but can be modeled with some strain–gradient plasticity theories. We evaluate the suitability of the strain–gradient plasticity theory developed by Fleck and Hutchinson to describe our experimental results in a continuum framework. Comparison between experimental results and calculations yields very good agreement for the effect of film thickness, but the strain–gradient plasticity model fails to describe the Bauschinger effect observed in passivated films.

© 2006 Acta Materialia Inc. Published by Elsevier Ltd. All rights reserved.

Keywords: Thin films; Plastic deformation; Bauschinger effect; Size effect

1. Introduction

Motivated by reliability problems encountered in engineering applications of thin films, research on thin-film plasticity provides a unique opportunity to improve our understanding of the deformation mechanisms in materials at small scales. A substantial amount of experimental work has shown that the plastic response of thin metal films is very different from that of their bulk counterparts. For example, the flow stress and hardening rate of thin films depend strongly on film thickness [1–8]. This size effect is usually attributed to dimensional and microstructural constraints on dislocation activity [9] that are not captured by classical plasticity theories. Various theoretical and numerical models have thus been proposed to

describe thin-film plasticity, including strain–gradient plasticity theories [10,11], crystal plasticity theories [12], molecular dynamics simulations [13], and discrete dislocation dynamics simulations [14,15]. Mechanisms for size effects in small-scale plasticity typically fall into one of two categories: (i) glide-control mechanisms, i.e., dislocation glide is constrained by the presence of geometrically necessary dislocations (GND) [10–12,14,16–26], either as a result of non-uniform deformation [7,27,28] or due to prescribed boundary conditions (e.g., [6,14]); and (ii) dislocation starvation mechanisms, where strengthening is due to the scarcity of dislocations that arises because of a lack of dislocation sources in small material volumes [7,29,30].

Besides the size effect associated with the film thickness, some models also predict unusual unloading behavior for thin films. For example, discrete dislocation simulations [31] predict a large Bauschinger effect in passivated films

* Corresponding author. Tel.: +1 617 496 0424; fax: +1 617 495 3897.
E-mail address: vlassak@esag.deas.harvard.edu (J.J. Vlassak).

during unloading, with significant reverse plastic flow even when the overall stress in the film is still in tension. Experimental evidence for such an unusual Bauschinger effect was not available until recently, when an experimental technique was developed by Xiang and Vlassak [32] to deform thin metal films alternating in tension and compression. Using this technique, a pronounced Bauschinger effect was observed in thin sputter-deposited Cu and Al films with one surface passivated using a thin ceramic coating. Unpassivated films, by contrast, showed little or no reverse plastic deformation when fully unloaded. The results were rationalized in terms of dislocation mechanics: a strong interface between the metal film and the ceramic layer prevents dislocations from exiting the film and results in significant back stresses; for unpassivated films, the free surface allows dislocations to exit the film and no back stresses are generated.

In this paper, we systematically investigate both the size effect and the Bauschinger effect in freestanding Cu thin films over a range of film thicknesses and surface passivation conditions. Specifically, the plane-strain bulge test technique is used to obtain the stress-strain curves as a function of surface passivation, film thickness and grain size. The experimental results are compared with calculations based on the strain-gradient plasticity theory developed by Fleck and Hutchinson [11].

2. Experiments

This section presents the sample preparation method and measurement technique. As described below, two sets of freestanding Cu films were prepared and investigated in this study. Set 1 consisted of freestanding electroplated Cu films with variable film thickness but constant microstructure. This set of films provides information on the effect of surface passivation and film thickness, while effects of microstructure have been ruled out. Set 2 consisted of freestanding, sputter-deposited Cu films with variable thickness and grain size. Half of these films had one of the surfaces passivated with a thin $\text{Si}_3\text{N}_4/\text{TaN}$ layer. This set of samples provides information on the Bauschinger effect in thin films, in addition to grain size and film thickness effects.

2.1. Experimental technique

The stress-strain curves of all films were obtained using the plane-strain bulge test technique [33,34]. In this technique, Si micromachining techniques are used to fabricate long rectangular freestanding membranes surrounded by a Si frame. These membranes are deformed in plane strain by applying a uniform pressure to one side of the membrane, as illustrated in Fig. 1. The stress and strain in the membrane are determined independently from the applied pressure, p , and the corresponding membrane deflection, δ , using the following expressions [34]:

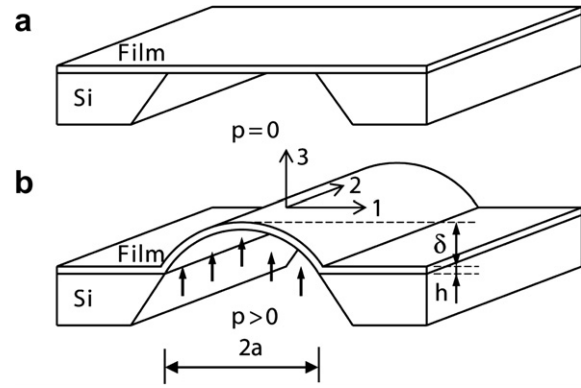


Fig. 1. Schematic illustration of the plane-strain bulge test. (a) Perspective view of a section of a freestanding membrane. The film is flat and under tension after sample preparation. (b) The film deflects when a uniform pressure is applied to one side of the freestanding membrane.

$$\sigma = \frac{p(a^2 + \delta^2)}{2\delta h} \quad \text{and} \quad (1)$$

$$\varepsilon = \varepsilon_0 + \frac{a^2 + \delta^2}{2a\delta} \arcsin\left(\frac{2a\delta}{a^2 + \delta^2}\right) - 1,$$

where h is the film thickness, $2a$ the width of the membrane, and ε_0 the residual strain in the film. Using this technique, it is possible to measure the plane-strain stress-strain curve of thin films if the aspect ratio of the membranes is larger than 4. Experiments were performed using a bulge test apparatus described in detail elsewhere in the literature [34]. The system has a displacement resolution of $0.3 \mu\text{m}$ and a pressure resolution of 0.1 kPa .

2.2. Sample preparation

The first set of samples consisted of electroplated Cu films with thickness varying from 1.0 to $4.2 \mu\text{m}$, but with constant microstructure (Table 1). These films were fabricated by electroplating $5.4 \mu\text{m}$ Cu films on Si substrates using a proprietary plating process. Prior to plating the Cu films, the Si substrates were coated with a 80 nm Si_3N_4 film using low-pressure chemical vapor deposition, a 20 nm TaN adhesion layer using reactive sputtering and a Cu seed layer using magnetron sputtering. The electroplated films were annealed at 400°C in vacuum for 15 min to obtain a uniform and stable microstructure. The films were subsequently thinned to the desired thickness by means of chemical mechanical polishing (CMP). Further details of the materials preparation process can be found in Ref. [6]. Freestanding Cu membranes were fabricated by opening long rectangular windows in the substrate using Si micromachining techniques [34] and by etching the exposed Si_3N_4 and TaN coatings using a CF_4 reactive plasma. Some of the Cu membranes were passivated by sputter coating 20 nm Ti onto either one surface or both surfaces.

The second set of samples consisted of sputter-deposited Cu films with thicknesses ranging from 0.34 to $0.89 \mu\text{m}$. For each thickness, Cu was sputtered directly onto free-

Table 1
Summary of the experimental results

Film set	Thickness h (μm)	Average grain size ^a d (μm)	h/d	Passivation ^b	Yield stress ^c σ_y (MPa)
First set, electroplated	4.20 \pm 0.05	1.50 \pm 0.05	2.80 \pm 0.13	Yes	181.8 \pm 3.5
				No	175.5 \pm 3.7
	1.90 \pm 0.05	1.51 \pm 0.04	1.26 \pm 0.07	Yes	212.6 \pm 4.5
				No	200.2 \pm 4.1
	1.00 \pm 0.05	1.50 \pm 0.05	0.67 \pm 0.04	Yes	250.8 \pm 5.4
No	200.5 \pm 4.2				
Second set, sputtered	0.89 \pm 0.01	0.46 \pm 0.02	1.93 \pm 0.11	Yes	335.5 \pm 16.8
				No	250.3 \pm 12.5
	0.67 \pm 0.01	0.46 \pm 0.01	1.43 \pm 0.05	Yes	373.6 \pm 16.7
				No	266.1 \pm 13.3
	0.61 \pm 0.01	0.54 \pm 0.02	1.14 \pm 0.06	Yes	434.6 \pm 21.7
				No	299.7 \pm 15.0
	0.44 \pm 0.01	0.39 \pm 0.01	1.13 \pm 0.05	Yes	611.7 \pm 30.6
No				346.6 \pm 17.3	
0.34 \pm 0.01	0.33 \pm 0.01	1.06 \pm 0.06	Yes	695.5 \pm 34.8	
			No	365.6 \pm 18.3	

^a The average grain size was determined by the intercept method with twins counted as separate grains.

^b The passivation consists of 20 nm Ti on both surfaces for electroplated films and 80 nm Si₃N₄/20 nm TaN on one surface for sputtered films.

^c The yield stress is defined at 0.2% offset strain for all films.

standing bilayer membranes that consisted of 80 nm of Si₃N₄ and 20 nm of TaN. Immediately prior to the Cu deposition, the TaN surface of the membranes was sputter-cleaned in situ using an Ar plasma. After deposition, all membranes were annealed in vacuum to increase the grain size of the films. Annealing temperatures were selected to ensure that the membranes would not buckle during the annealing step as a consequence of the differential thermal expansion between the membrane and the Si frame. The resulting grain sizes were measured using plan-view transmission electron microscopy and are listed in Table 1. For some samples, the Si₃N₄/TaN layer was etched away using a reactive ion etch (RIE) in order to create freestanding Cu membranes. Other samples were tested as annealed without removing the Si₃N₄/TaN layer. The reason for leaving the thin Si₃N₄/TaN layer in place is two-fold. First, the Si₃N₄/TaN layer serves to passivate one of the surfaces of the Cu film by blocking dislocations from exiting the film. Comparison of the stress–strain curves of these films with those of unpassivated freestanding Cu films provides information on the effect of a free surface or interface on the mechanical behavior of thin films. The second reason for leaving the Si₃N₄/TaN layer in place is that this layer makes it possible to alternate the direction of plastic flow in the Cu film during a bulge test experiment [32]. This is realized by first loading the composite membrane in the bulge test until the Cu flows plastically. The Si₃N₄/TaN layer only deforms elastically and a large tensile stress is built up in this layer. Upon unloading, the tensile stress in the Si₃N₄/TaN drives the Cu film into compression, while the overall stress in the composite membrane is kept tensile to prevent buckling of the membrane. The stress–strain curve of the Cu film is then obtained by subtracting the elastic contribution of the Si₃N₄/TaN coating from the stress–strain curve of the composite film. The contribution

of the Si₃N₄/TaN coating is readily determined by bulge testing the membrane after the Cu film has been dissolved in dilute nitric acid. It should be noted that this technique circumvents the problem of buckling when testing freestanding thin films in compression because the average stress in the membrane is kept tensile. As such, it is the only technique currently available to test the same freestanding film in tension and compression.

3. Experimental results

3.1. Microstructure

The grain structure of the electroplated samples was characterized using both plan-view focused ion beam (FIB) microscopy and cross-section transmission electron microscopy (TEM). Electroplated Cu films typically have a high incidence of twins, e.g., Fig. 2(a) and Ref. [35], and twin boundaries are effective internal obstacles to dislocation motion [35–37]. Therefore, the average grain size in the plane of the film was determined by the intercept method with twins counted as separate grains. As listed in Table 1, the average grain size of the films is 1.5 μm independent of film thickness. By contrast, if regular grains are counted, the average grain size of the films is approximately 2.7 μm . X-ray diffraction shows that the crystallographic texture of the films is also independent of thickness. A typical orientation distribution function is shown in Fig. 2(b). The texture consists of distinct $\langle 111 \rangle$, $\langle 110 \rangle$ and $\langle 100 \rangle$ fiber components as well as a random component. Cross-section TEM (Fig. 3) reveals that the thinnest electroplated films have a grain size of the order of the film thickness with grain boundaries traversing the entire film (Fig. 3(a)); thick films typically have more than one grain through the thickness (Fig. 3(b)). This is not

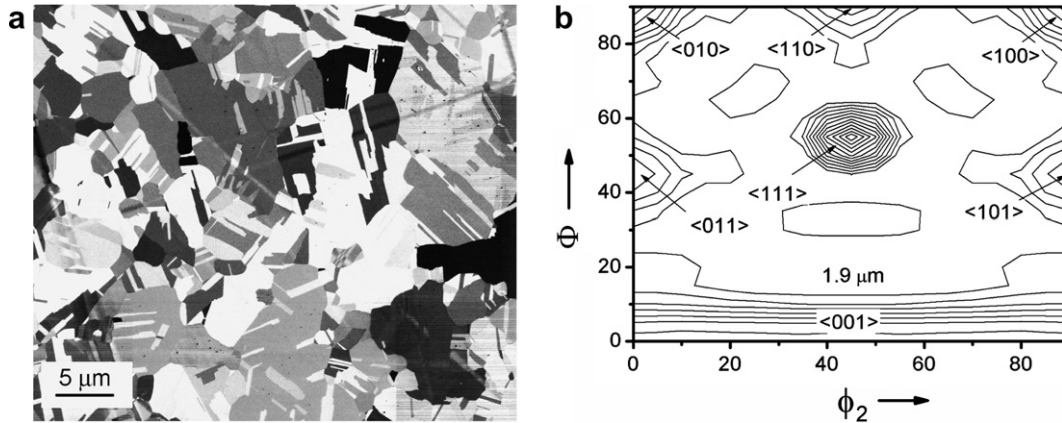


Fig. 2. (a) A typical focused ion beam plan-view micrograph and (b) a typical orientation distribution function of an electroplated 1.9 μm Cu film.

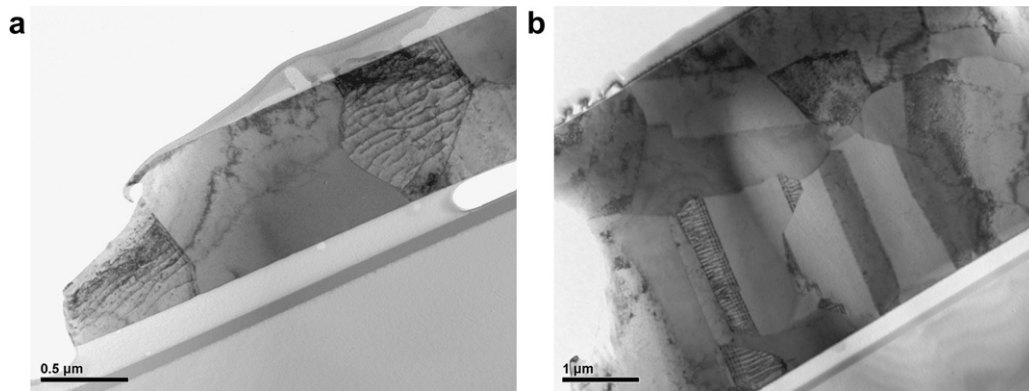


Fig. 3. Cross-section transmission electron micrographs of electroplated Cu films showing: (a) a grain size on the order of the film thickness for a 1.0 μm film; (b) more than one grain across the film thickness for a 4.2 μm film.

surprising given that the average grain size of the electroplated films is approximately one-third the thickness of the thickest film.

The grain structure of the sputtered films was characterized using plan-view TEM. The films have a columnar grain structure with grains that are equi-axed in the plane of the film. Fig. 4 shows typical TEM micrographs for the thinnest (0.34 μm) and the thickest (0.89 μm) films. The grain size of the sputtered films is a weak function of

film thickness (see Table 1). The sputtered films have a mixed texture that consists mainly of (111) and (100) fiber components, with the (100) component slightly weaker for the thinner films. In order to quantify the effect of crystallographic texture on the mechanical behavior of the films, the plane-strain tension Taylor factors of the films were calculated from the experimental orientation distribution functions as described in Ref. [35]. The Taylor factors of the sputtered films vary by less than 2% with film thickness,

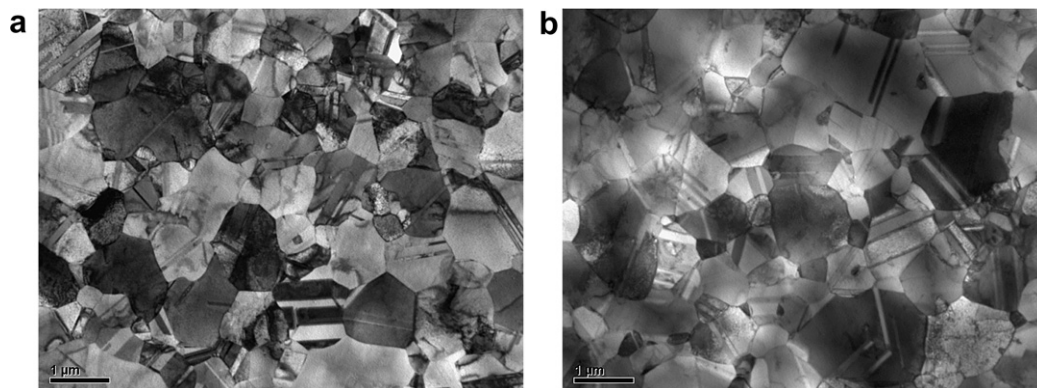


Fig. 4. Plan-view transmission electron micrographs showing typical grain structures for (a) a 0.34 μm and (b) a 0.89 μm sputter-deposited Cu film.

while the difference in Taylor factor between the electroplated and sputtered films is at most 5%. Consequently, the small differences between the crystallographic textures of the Cu films used in this study do not have a significant impact on the mechanical behavior of the films.

3.2. Stress–strain curves

Typical stress–strain curves for the electroplated Cu films are presented in Fig. 5. Fig. 5(a) shows the effect of the Ti passivation layer on the stress–strain curve of a 1.0 μm Cu film; Fig. 5(b) and (c) illustrates the effect of Cu thickness for unpassivated films and for films with both surfaces passivated by 20 nm of Ti, respectively. For a given film thickness, the passivation layer clearly increases the work-hardening rate of the film. Furthermore, the stress–strain curves of passivated films vary markedly with film thickness, even though the microstructure of the films is unchanged. This needs to be contrasted with the behavior of unpassivated films, which show much less variation with film thickness.

Fig. 6 shows typical stress–strain curves for sputtered films with thicknesses varying from 0.34 to 0.89 μm . For each thickness, results are shown for both films with and without $\text{Si}_3\text{N}_4/\text{TaN}$ passivation. Films with passivation have a significantly larger flow stress than unpassivated films. This increased flow stress is not due to the stress in the $\text{Si}_3\text{N}_4/\text{TaN}$ layer, because the contribution of this layer

was removed from the data as explained in Section 2.2. All passivated films with the exception of the thinnest films are deformed in compression at the end of the last few unloading cycles. All unloading/reloading cycles for these passivated films show significant hysteresis with reverse plastic flow occurring even when the overall stress in the films is still tensile. By contrast, films without passivation show little or no reverse plastic deformation when fully unloaded. In other words, passivated films show a strong Bauschinger effect, while unpassivated films do not. It should be noted that the stress–strain curves of the electroplated films with Ti passivation show only a small Bauschinger effect. From Fig. 6, it is evident that the Bauschinger strain during an unloading cycle increases with increasing pre-strain and unloading strain. Thus, we attribute the small Bauschinger strains observed for the passivated electroplated films to the relatively small values of pre-strain and unloading strain of the unloading cycles for these films.

3.3. Yield stress

Table 1 lists the yield stress (defined at 0.2% offset strain) for all films tested. Fig. 7(a) presents the yield stress of both passivated (filled symbols) and unpassivated (open symbols) films as a function of inverse film thickness. The vertical line divides the data for the electroplated and the sputtered films.

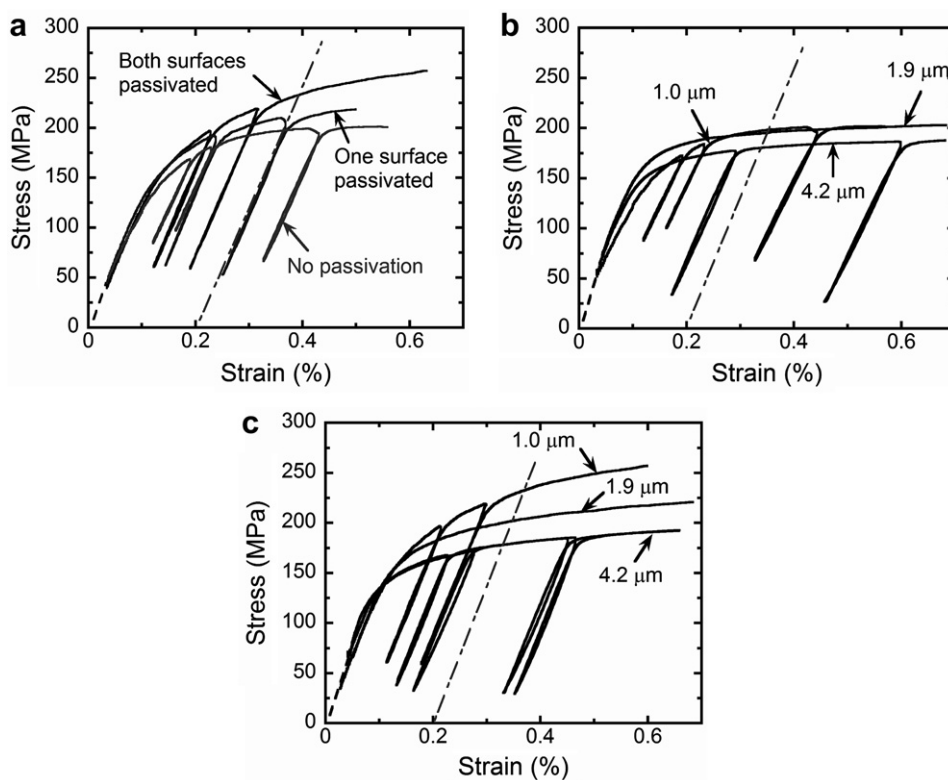


Fig. 5. (a) The effect of passivation on the stress–strain curves of 1.0 μm electroplated Cu films. (b) The effect of film thickness on the stress–strain curves of electroplated Cu films without surface passivation. (c) The effect of film thickness on the stress–strain curves of electroplated Cu films with both surfaces passivated by 20 nm of Ti. All curves are offset by the equi-biaxial residual strain in the films, as represented by the dashed lines starting at the origins.

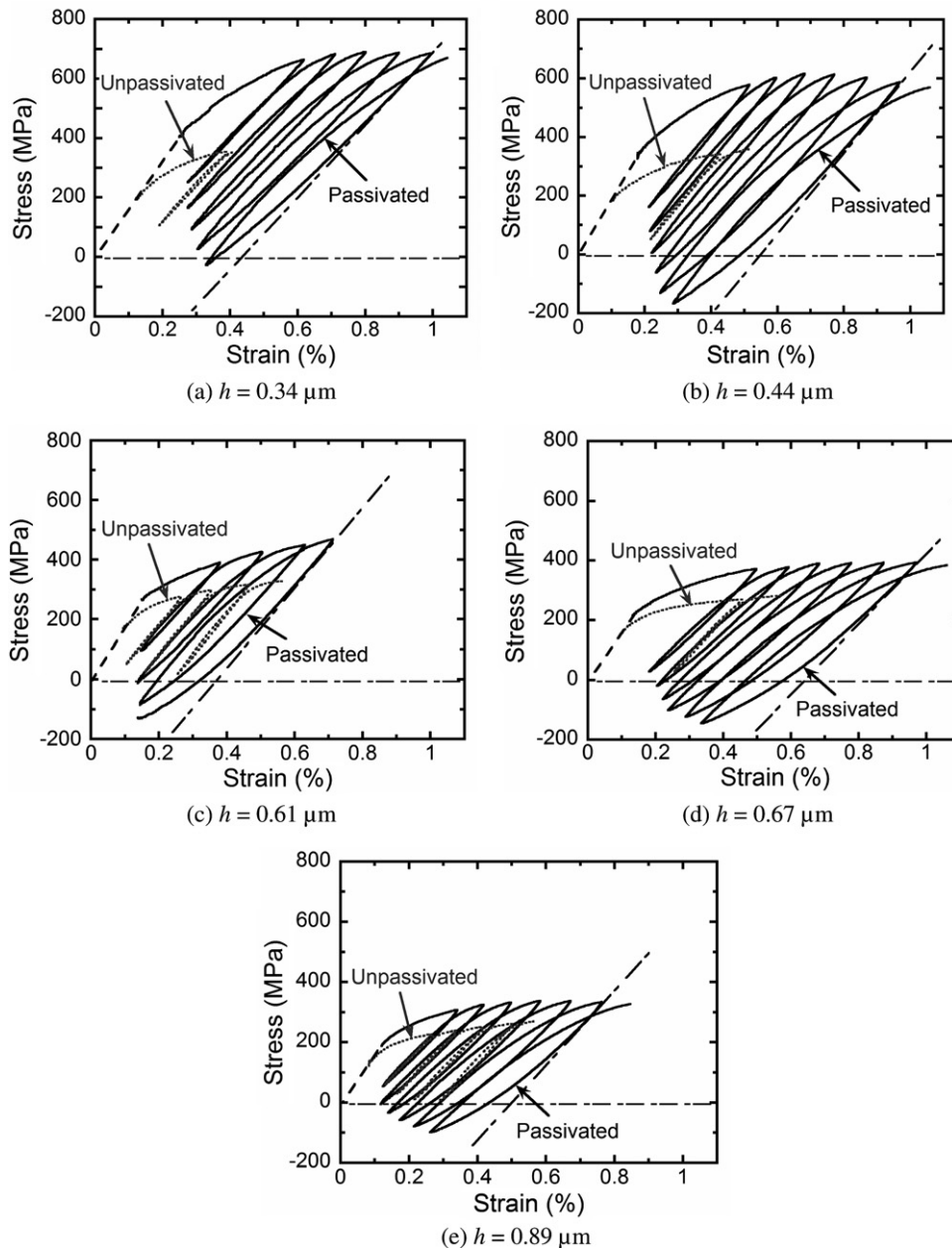


Fig. 6. Typical stress–strain curves for unpassivated (dotted curves) and passivated (solid curves) sputtered Cu films of thickness h . All curves are plotted to the same scale and are offset by the equi-biaxial residual strains in the films, as represented by the dashed lines starting at the origins.

The yield stress of the sputter-deposited films without passivation increases with decreasing film thickness, although not as much as for the sputtered films with passivation. The rise in the yield stress of the unpassivated films is the result of Hall–Petch hardening: thinner films have a smaller grain size (Table 1) and hence a higher yield stress. The effect of grain size is better appreciated by plotting the yield stress of the unpassivated sputtered and electroplated films as a function of the reciprocal square root of the average grain size, as illustrated in Fig. 7(b). Also plotted are the data for freestanding electroplated Cu films from a previous study [35] and a linear fit (solid line) of the Hall–Petch relationship to the data. The Hall–Petch slope is

$0.19 \text{ MPa m}^{1/2}$, which is in good agreement with the value for bulk Cu, considering that the results in Fig. 7(b) are for plane strain. It is evident that the three sets of experimental results in the figure are in reasonable agreement, independent of the film deposition technique.

The data in Table 1 and in Fig. 7(a) show that a passivation layer increases the yield stress of a passivated Cu film above that of an unpassivated film of the same grain size and thickness, and that this effect is much more significant for the sub-micron films passivated by a $\text{Si}_3\text{N}_4/\text{TaN}$ layer than for the thicker films passivated by Ti. It is not clear at this point whether this is so because the Ti passivation provides less of a constraint on dislocation motion than

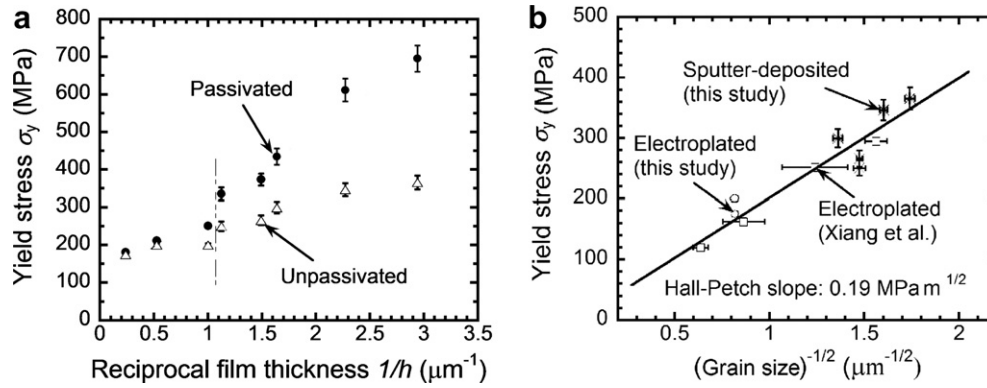


Fig. 7. (a) Yield stress of both passivated (filled symbols) and unpassivated (open symbols) Cu films as a function of inverse film thickness. (b) Yield stress of unpassivated films is correlated with the average grain size through a distinct Hall–Petch behavior.

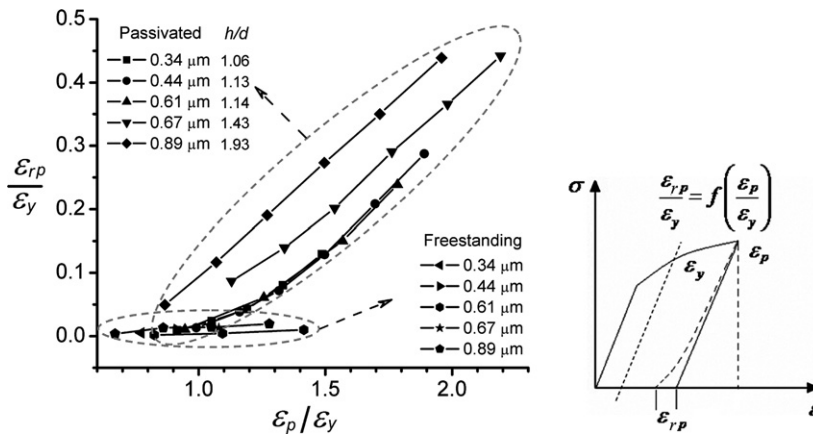


Fig. 8. Bauschinger effect in sputtered Cu films: the reverse plastic strain, ϵ_{rp} , as defined in the inset, is plotted as a function of the applied pre-strain, ϵ_p . Both strains are normalized by the yield strain, $\epsilon_y = \sigma_y (1 - \nu^2)/E$, where σ_y is the yield stress defined at 0.2% offset strain.

the $\text{Si}_3\text{N}_4/\text{TaN}$ layer or because the effect of the passivation is indeed much more pronounced at small film thicknesses. We will address this issue in more detail in Section 5.

3.4. Bauschinger effect

In order to compare the Bauschinger effect in passivated and unpassivated films quantitatively, the reverse plastic strain at the end of each unloading cycle, ϵ_{rp} , is plotted as a function of total prestrain, ϵ_p , in Fig. 8. Both strains are normalized by the yield strain of the films, ϵ_y , as defined in the inset of Fig. 8. The difference between passivated and unpassivated films is immediately evident. Moreover, grain size and film thickness seem to have a strong effect on the reverse flow in passivated films.

4. Strain–gradient plasticity description

In this section, we use strain–gradient plasticity (SGP) theory to describe our experimental results in a continuum framework. The use of strain–gradient plasticity theory is motivated by the fact that a well-adhered passivating layer prevents dislocations from exiting the film and leads to a

plastic strain gradient near the film–passivation interface. The constraint on plastic flow imposed by a passivating layer cannot be described by classical plasticity theories, but can be modeled with some strain–gradient plasticity theories. A direct comparison of our experimental results with discrete dislocation simulations is presented in a separate paper [29] and provides more insight in the precise deformation mechanisms at work.

4.1. A brief introduction to strain–gradient plasticity

One of the recognized sources for the size effect in plasticity at the micron scale is the presence of plastic strain gradients that increase the resistance to plastic flow by locally increasing the dislocation density. This feature is not captured by classical plasticity theories and leads naturally to the introduction of one or more material length parameters. These length parameters set the characteristic dimensions of the deformation field at which the contribution of plastic strain gradients to work hardening is comparable to that of plastic strains. Work hardening due to dislocation interactions is quantified by the empirical Taylor model, which relates the flow stress to

the total dislocation density in the material. Dislocations can be divided into so-called statistically stored dislocations (SSDs) and geometrically necessary dislocations (GNDs). The two types of dislocations are physically indistinguishable in a crystal and contribute to Taylor hardening in the same way, i.e., both types of dislocations are internal obstacles to gliding dislocations. Generally, SSDs are associated with the macroscopic plastic strains in the material, while GNDs have a net Burgers vector in a given volume and arise as a result of plastic strain gradients.

The strain–gradient plasticity theories in the literature are typically categorized depending on how plastic strain gradients are incorporated into the theories. In this paper, we briefly introduce the stretch and rotation version of strain–gradient plasticity theory proposed by Fleck and Hutchinson; a complete discussion can be found in Ref. [11]. This theory is a generalization of classical J_2 theory in both flow and deformation versions. The dependence on plastic strain gradients is incorporated by introducing a generalized effective plastic strain, which is a weighted function of the conventional effective plastic strain and three independent invariants of the plastic strain gradient tensor. The three material length parameters (ℓ_1 , ℓ_2 and ℓ_3) that enter the coefficients of the three independent invariants characterize the contributions of the stretch and rotation gradients of the plastic strains to the resistance to plastic flow. In particular, ℓ_2 and ℓ_3 determine the contribution of rotation gradients, while ℓ_1 reflects the contribution of both stretch and rotation gradients. The essence of the Fleck–Hutchinson theory is that the generalized effective plastic strain is used as a phenomenological measure of the total dislocation density resulting from plastic strains (SSDs) and their gradients (GNDs) and that both types of dislocations increase the plastic flow resistance in the same way.

4.2. Problem formulation

The plastic response of a homogeneous, isotropic thin film in the bulge test configuration is analyzed using the flow version of the Fleck–Hutchinson theory. Fig. 9 schematically illustrates the cross-section of the film. The plastic flow is constrained at the bottom surface of the film due to the presence of the passivation layer. We choose a Cartesian coordinate system with origin at the film–passivation interface and with three axes along the three principal stress directions (cf. Fig. 1). The film is subjected to plane–strain tension with the strain rate along the longitudinal direction, $\dot{\epsilon}_{22}$, equal to zero. Moreover, since the pressure applied to the film is much smaller compared to the in-plane stress, the stress rate normal to the film surface, $\dot{\sigma}_{33}$, can be taken equal to zero. In order to avoid mathematical complexity, the plastic strain in the x_2 -direction is also set to zero. This simplification has negligible influence for calculations in the plastic regime [11]. The plastic strain rate components are functions of $x_3 \equiv z$ only and can be

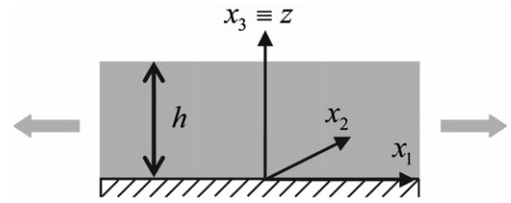


Fig. 9. Schematic illustration of the cross-section of a thin film under plane–strain tension. The bottom surface of the film is passivated by a hard layer that deforms elastically, but not plastically. The x_2 -axis points into the plane of the page.

expressed in terms of the conventional effective plastic strain rate, $\dot{\epsilon}_p = \sqrt{2\dot{\epsilon}_{ij}^p\dot{\epsilon}_{ij}^p}/3$,

$$\dot{\epsilon}_{11}^p(z) = -\dot{\epsilon}_{33}^p(z) = \frac{\sqrt{3}}{2}\dot{\epsilon}_p(z), \quad \dot{\epsilon}_{22}^p(z) = 0, \quad (2)$$

where $\dot{\epsilon}_{11}^p$ is the plastic part of the applied strain rate, $\dot{\epsilon}_{11}$, and the corresponding elastic strain rate is $\dot{\epsilon}_{11}^e = \dot{\epsilon}_{11} - \dot{\epsilon}_{11}^p$. The generalized effective plastic strain rate, \dot{E}_p , is found to be

$$\dot{E}_p^2 = \dot{\epsilon}_p^2 + \left(\frac{1}{2}\ell_1^2 + \frac{8}{3}\ell_3^2\right)\dot{\epsilon}_p'^2 = \dot{\epsilon}_p^2 + \ell^2\dot{\epsilon}_p'^2, \quad (3)$$

where $(\prime) \equiv \frac{d(\)}{dz}$, ℓ_1 and ℓ_3 are material length parameters originally defined in Ref. [11], and $\ell = \sqrt{\frac{1}{2}\ell_1^2 + \frac{8}{3}\ell_3^2}$ is an effective length parameter that sets the scale at which the contribution of the gradient term is important to the generalized effective plastic strain rate for this problem. The second material length parameter, ℓ_2 , does not enter the expression. The stress rate components are given in terms of the conventional equivalent stress rate, $\dot{\sigma}_e = \sqrt{2\dot{s}_{ij}\dot{s}_{ij}}/3$, with \dot{s}_{ij} the stress deviator:

$$\dot{\sigma}_{11} = 2\dot{\sigma}_{22} = \frac{2}{\sqrt{3}}\dot{\sigma}_e, \quad \dot{\sigma}_{33} = 0. \quad (4)$$

The constitutive equation in the strain–gradient plasticity theory is

$$\dot{\sigma}_e = \dot{h}(E_p)\dot{\epsilon}_p - \ell^2(\dot{h}(E_p)\dot{\epsilon}_p')', \quad (5)$$

where $\dot{h}(E_p)$ is the tangent hardening quantity of the uniaxial tensile stress–strain curve, $d\sigma(\epsilon_p)/d\epsilon_p$, evaluated at the generalized effective plastic strain rate, \dot{E}_p . In the calculations, the equivalent uniaxial tensile stress–strain curves of the films are used as input to the formulation and we use the Ramberg–Osgood curve,

$$\frac{\epsilon}{\epsilon_0} = \frac{\sigma}{\sigma_0} + \left(\frac{\sigma}{\sigma_0}\right)^N \quad \text{or} \quad \sigma = \sigma_0\left(\frac{\epsilon_p}{\epsilon_0}\right)^{1/N}, \quad N = \frac{1}{n}, \quad (6)$$

where ϵ_0 and σ_0 are the yield strain and yield stress, respectively, $\epsilon_0 = \sigma_0/E$, and E is Young's modulus. Thus $\dot{h}(E_p)$ is equal to $NE(E_p/\epsilon_0)^{N-1}$. For convenience, the strain and stress rates are normalized by ϵ_0 and σ_0 , with $\dot{\tilde{\epsilon}}_{11} = \dot{\epsilon}_{11}/\epsilon_0$, $\dot{\tilde{\epsilon}}_{11}^p = \dot{\epsilon}_{11}^p/\epsilon_0$, $\dot{\tilde{\epsilon}}_{11}^e = \dot{\epsilon}_{11}^e/\epsilon_0$, $\dot{\tilde{\epsilon}}_p = \dot{\epsilon}_p/\epsilon_0$, $\dot{\tilde{E}}_p = \dot{E}_p/\epsilon_0$, $\dot{\tilde{\sigma}}_{11} = \dot{\sigma}_{11}/\sigma_0$, and $\dot{\tilde{\sigma}}_e = \dot{\sigma}_e/\sigma_0$; ℓ and z are normalized by the film thickness, h , with $L = \ell/h$, $x = z/h$, and $\frac{d(\)}{dz} = \frac{1}{h}\frac{d(\)}{dx}$.

For simplicity, from now on we denote $(\dot{\epsilon})' \equiv \frac{d(\dot{\epsilon})}{dx}$. Substituting $\dot{h}(E_p) = NE_p/\epsilon_0)^{N-1}$ into Eq. (5), we find

$$\dot{\sigma}_e = N\dot{E}_p^{N-1}\dot{\epsilon}_p - L^2\left(N\dot{E}_p^{N-1}\dot{\epsilon}_p^2\right)', \quad (7)$$

where $\dot{E}_p = \left(\dot{\epsilon}_p^2 + L^2\dot{\epsilon}_p^2\right)^{1/2}$ is the normalized effective plastic strain rate from Eq. (3). From Eqs. (2) and (4) and noticing that $\dot{\epsilon}_{11}^e = \dot{\epsilon}_{11} - \dot{\epsilon}_{11}^p$, the effective stress rate can be related to the applied strain rate, $\dot{\epsilon}_{11}$, and the conventional effective strain rate, $\dot{\epsilon}_p$, which is the quantity of interest,

$$\begin{aligned} \dot{\sigma}_e &= \frac{\sqrt{3}}{2}\dot{\sigma}_{11} = \frac{\sqrt{3}}{2(1-\nu^2)}\dot{\epsilon}_{11}^e = \frac{\sqrt{3}}{2(1-\nu^2)}(\dot{\epsilon}_{11} - \dot{\epsilon}_{11}^p) \\ &= \frac{\sqrt{3}}{2(1-\nu^2)}\left(\dot{\epsilon}_{11} - \frac{\sqrt{3}}{2}\dot{\epsilon}_p\right) \end{aligned} \quad (8)$$

If we denote $y_1 = \dot{\epsilon}_p$, $y_2 = \dot{\epsilon}'_p$, Eqs. (7) and (8) yield the following ordinary differential equations:

$$y_1' = y_2; \quad y_2' = \frac{A-B}{C}, \quad (9)$$

where $A = \frac{1}{L^2}\left(\dot{\epsilon}_p - \dot{\sigma}_e\dot{E}_p^{1-N}\right)$, $B = \frac{N-1}{E_p^2}\dot{\epsilon}_p\dot{\epsilon}_p^2$, and $C = \frac{N-1}{E_p^2}\left(L^2\dot{\epsilon}_p^2 + 1\right)$. The boundary conditions are

$$y_1|_{x=0} = \dot{\epsilon}_p|_{x=0} = 0; \quad y_2|_{x=1} = \dot{\epsilon}'_p|_{x=1} = 0. \quad (10)$$

Here a condition of no plastic flow is enforced at the film–passivation interface ($x = 0$), while a condition of no plastic strain gradient is imposed at the free surface ($x = 1$). These boundary conditions are the mathematical representation of the fact that a free surface allows dislocations to escape, while a well-adhered passivating layer is an effective dislocation barrier. If both surfaces of the films are passivated, the boundary condition Eq. (10) needs to be replaced by

$$y_1|_{x=0} = y_1|_{x=1} = 0, \quad (11)$$

while all other equations remain the same. This boundary value problem (Eq. (9), and Eqs. (10) or (11)) can be solved incrementally to obtain the stress–strain curve using numerical methods. In this study, we used the built-in ordinary differential function solver, bvp4c.m, in Matlab.

4.3. Strain–gradient plasticity results

The stress–strain curves of the unpassivated sputter-deposited films (second set of samples) are used to derive the stress–strain curves of the Si₃N₄/TaN passivated films based on the strain–gradient plasticity formulation in the previous section. Since the stress–strain curves of the unpassivated films are best fitted with a work-hardening coefficient N between 0.1 and 0.15, the lower and upper

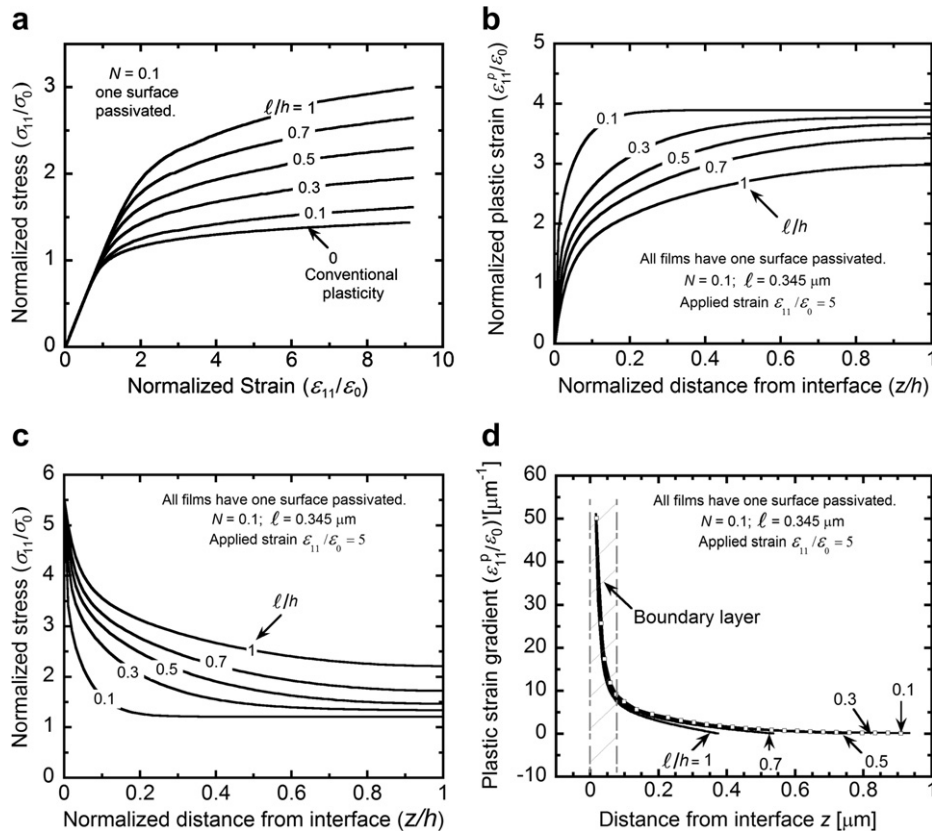


Fig. 10. (a) Calculated stress–strain curves for films with one surface passivated ($N = 0.1$). (b) Distribution of plastic strain across the film thickness. (c) Distribution of stress across the film thickness. (d) A layer with high plastic strain gradients is formed near the film–passivation interface. The width of this layer is nearly independent of film thickness.

bounds to the stress–strain curves of passivated films are calculated using the two limiting values of N . Fig. 10(a) presents typical results for films with one surface passivated for $N = 0.1$ and for several values of ℓ/h . The size effect is clearly shown in the stress–strain curves: the flow stress and work-hardening rate increase with decreasing film thickness h . Fig. 10(b) and (c) compares the distribution of the transverse plastic strain ε_{11}^p and transverse stress σ_{11} across the film thickness, respectively. It should be noted that the plastic strain is zero at the film–passivation interface. This is a boundary condition that cannot be enforced in conventional plasticity. Fig. 10(d) shows the plastic strain gradient as a function of the distance from the interface. It is evident that a layer with large gradients of plastic strains exists near the film–passivation interface and that the width of this layer is nearly independent of the film thickness.

In order to compare the model results with the experimental data, we define a strengthening factor S that characterizes the effect of the passivation

$$S = \sigma_y^p / \sigma_y^u, \quad (12)$$

where σ_y^p and σ_y^u are the yield stress for a film of given thickness with and without passivation, respectively. Since films with identical microstructure are compared, S reflects solely the effect of the passivation. The strengthening factor is calculated from both the experimental (Fig. 6(a)–(e)) and the model (Fig. 10(a)) stress–strain curves and is plotted as a function of film thickness in Fig. 11. The value of the length parameter ℓ can be obtained by fitting the model results (dashed and solid curves) to the experimental data points (filled squares), where the dashed and solid curves correspond to the two limiting cases with $N = 0.1$ and 0.15, respectively. The corresponding values of the material length parameter are $\ell = 360$ nm and 330 nm, representing an upper and lower limit, respectively. The average of the two values can be taken as the value of ℓ for the films.

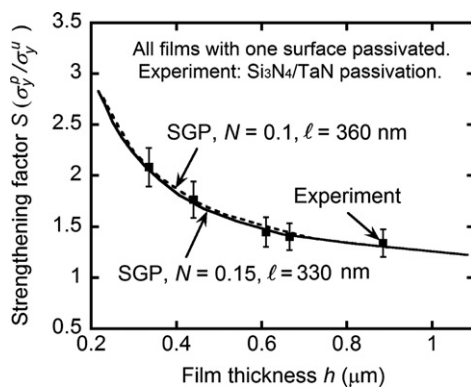


Fig. 11. The strengthening factor, S , as defined in Eq. (12), versus the film thickness. The dashed line is the best fit to experimental data with a length scale parameter $\ell = 0.36 \mu\text{m}$ for a hardening index $N = 0.15$, while the solid line is the best fit with $\ell = 0.33 \mu\text{m}$ for $N = 0.1$.

5. Comparison and discussion

5.1. Size effect

Because the $\text{Si}_3\text{N}_4/\text{TaN}$ passivation layer deforms only elastically and adheres well to the Cu film, it is assumed in the SGP model that plastic flow is completely suppressed at the film–passivation interface—only elastic strains are allowed. Consequently, the calculations show that the passivated films have a layer with a large plastic strain gradient near the film–passivation interface. As is evident in Fig. 10(d), the width of this layer is nearly independent of the film thickness. Thus, for the same applied total strain, the average plastic strain in a thin film is smaller than in a thick film, while the level of stress is larger. This observation gives rise to the thickness-dependent plastic behavior in the SGP model. The SGP explanation is consistent with the presence of a boundary layer with high dislocation density near the film–passivation interface as suggested by some discrete dislocation simulations [14] and TEM observations [6]. This boundary layer forms naturally as the film–passivation interface prevents dislocations from exiting the film. The connection with strain–gradient plasticity is made through the observation that the dislocation pile-ups and the more complex dislocation structures that form at the film–passivation interface must have a net Burgers vector, which in turn results in a plastic strain gradient.

The plastic strain gradient that arises at the interface with the passivating layer can be very large, as indicated in Fig. 10(d). The corresponding average spacing between dislocations in a slip band is small—of the order of a few tens of nanometers in the present case. When the film continues to be strained, the dislocation spacing decreases further and the stress ahead of the slip bands increases. At some point, this stress is large enough to induce plasticity or fracture in the passivating layer or debonding of the interface. When this happens, the passivation layer is no longer an effective barrier to dislocation motion and the boundary condition of no plastic flow at the interface ceases to be valid; the mechanism described above breaks down and a reduced dependence of the flow stress on the film thickness is expected.

By comparing the yield stress of the sputtered films with the strain–gradient plasticity calculations in Fig. 11, we obtained a value of $\ell = 0.345 \pm 0.015 \mu\text{m}$ for the films. Values for both ℓ_1 and ℓ_2 have been reported in the literature. Length scale ℓ_1 , which describes the effects of both plastic stretch and rotation gradients, is typically in the range 0.2–0.5 μm [11,38]; ℓ_2 , which defines the effect of plastic rotation gradients, is of the order of 2 μm [11]. Little or no information is available on ℓ_3 , which also is a measure for the effect of rotation gradients. The relevant length scale in the problem at hand depends on both ℓ_1 and ℓ_3 :

$$\ell = \sqrt{\frac{1}{2}\ell_1^2 + \frac{8}{3}\ell_3^2}.$$

The experimental results do not allow independent determination of l_1 and l_3 , but they do imply that l_3 is possibly of the same order of magnitude as l_1 and small compared to l_2 .

The significance of l in the present problem is obvious from Eq. (3): if the characteristic dimension of the deformation field, or more specifically the film thickness in the current problem, is equal to l , then the contribution of the plastic strain gradients to the flow stress is of the same order of magnitude as that of the plastic strains. This contribution is evident in Fig. 10(a) when the film thickness approaches l .

According to Fig. 7(a), the dependence of the yield stress of the passivated films on film thickness seems to be somewhat different for films with thickness below or above 1 μm . We now examine the two explanations mentioned in Section 3.3. Using the value of l obtained from the sputtered films, one can calculate the strengthening factors for films passivated on both sides and compare them with the experimental values. The model and experimental values are within experimental error, indicating that the reduced strengthening in the Ti-passivated films is not caused by the nature of the passivating layer, i.e., there is no plasticity in the Ti passivation layers at low strain levels, but by the larger film thickness. It should finally be noted that the Ti-passivated films are electroplated films with a much larger grain size than the $\text{Si}_3\text{N}_4/\text{TaN}$ -passivated films. This effect also reduces their yield stress as is evident in Fig. 7(a).

5.2. Bauschinger effect

Fig. 10(c) shows that the stress distribution in passivated films is very non-uniform. It is conceivable that this non-uniform stress distribution could cause reverse plastic flow even if the average stress in the film is still tensile. Such behavior would result in a Bauschinger effect in the stress–strain curves of the passivated films. In order to evaluate this possibility, the strain gradient theory was used to calculate the unloading curves of the films. A typical stress–strain curve with unloading segment is shown in Fig. 12. Although there certainly is some asymmetry in the stress–strain curve as the film is loaded in compression, it is evident from the figure that no significant reverse flow occurs upon unloading. Therefore, the Bauschinger effect as observed experimentally is not predicted by the strain gradient plasticity calculations. The non-uniform plastic strain distribution (Fig. 10(b)) and its gradient (Fig. 10(d)) suggest, however, the following mechanism for the Bauschinger effect observed in these experiments. The large plastic strain gradient indicates that a large number of GNDs are present near the interface. The net Burgers vector of the GNDs leads to a directional back stress on the dislocations. This back stress causes flow asymmetry and the Bauschinger effect found in the stress–strain curves. This observation would argue for the inclusion of a back stress in the Fleck–Hutchinson theory. Such a back stress would naturally lead to a certain degree of kinematic hardening

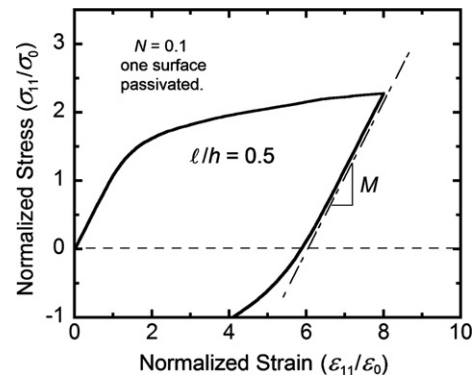


Fig. 12. Calculated stress–strain curves with an unloading section for a 0.69 μm film.

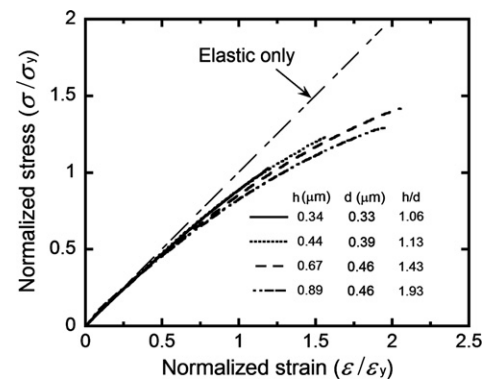


Fig. 13. Normalized final unloading curves of passivated, sputter-deposited Cu films. Stress and strain have been normalized by the yield stress and the yield strain, $\epsilon_y = \sigma_y (1 - \nu^2)/E$, of each film, respectively.

and could be used to describe the Bauschinger effect in thin films.

Fig. 13 shows the final unloading curves of a number of passivated films after shifting the initial unloading point to the origin and changing the signs of stress and strain. Stress and strain have been normalized by the yield stress and yield strain of each film, respectively. This simple procedure causes all unloading curves for a given film to collapse and makes it easier to evaluate how the Bauschinger effect varies from film to film. The tight distribution of the final unloading curves in Fig. 13 suggests that the normalized curves are relatively independent of film thickness and microstructure, i.e., the effect of these parameters on reverse flow during unloading scales directly with the yield stress of the films. Since the yield stress of passivated films increases with decreasing film thickness, so does the Bauschinger effect. It should be noted, however, that the normalization used in Fig. 13 only works for films with similar loading histories. If the loading history is different, the spread in the unloading curves increases.

6. Conclusions

Stress–strain curves of Cu films with thicknesses ranging from 0.34 to 4.2 μm and with various surface passivation

conditions have been obtained using the plane-strain bulge test technique. Passivated films show a strong film thickness effect on loading and a distinct Bauschinger effect on unloading due to build-up of significant back stresses near the film-passivation interfaces. By contrast, unpassivated films show a negligible Bauschinger effect on unloading. The yield stress of unpassivated films varies with film thickness mainly due to a change of grain size, as described by the Hall–Petch relation. The experimental results are compared with strain-gradient plasticity calculations based on the theory developed by Fleck and Hutchinson. This theory provides a good description of the film-thickness effect in the passivated films, but does not capture the Bauschinger effect.

Acknowledgements

The authors are grateful to M.T. Perez-Prado for assistance with the XRD characterization, X. Wang for help with the TEM work and T.Y. Tsui for providing the electroplated films. Helpful discussions with F. Spaepen and Z. Zhang are also gratefully acknowledged. Discussions with J.W. Hutchinson were instrumental to the formulation of the strain-gradient plasticity problem. This work was funded by the National Science Foundation under grant DMR-0133559 and by the Materials Research Science and Engineering Center of the National Science Foundation under NSF Award Number DMR-0213805.

References

- [1] Nix WD. *Metall Trans A* 1989;20:2217.
- [2] Vinci RP, Vlassak JJ. *Annu Rev Mater Sci* 1996;26:431.
- [3] Venkatraman R, Bravman JC. *J Mater Res* 1992;7:2040.
- [4] Shen YL, Suresh S, He MY, et al. *J Mater Res* 1998;13:1928.
- [5] Keller R, Baker SP, Arzt E. *J Mater Res* 1998;13:1307.
- [6] Xiang Y, Vlassak JJ, Perez-Prado MT, et al. *Mater Res Soc Symp Proc* 2004;795:417.
- [7] Haque MA, Saif MTA. *Acta Mater* 2003;51:3053.
- [8] Espinosa HD, Prorok BC, Peng B. *J Mech Phys Solids* 2004;52:667.
- [9] Arzt E. *Acta Mater* 1998;46:5611.
- [10] Triantafyllidis N, Aifantis EC. *J Elast* 1986;16:225.
- [11] Fleck NA, Hutchinson JW. *J Mech Phys Solids* 2001;49:2245.
- [12] Bittencourt E, Needleman A, Gurtin ME, et al. *J Mech Phys Solids* 2003;51:281.
- [13] Schiotz J, Di Tolla FD, Jacobsen KW. *Nature* 1998;391:561.
- [14] Nicola L, Van der Giessen E, Needleman A. *J Appl Phys* 2003;93:5920.
- [15] Nicola L, Van der Giessen E, Needleman A. *Mater Sci Eng A* 2001;309:274.
- [16] Aifantis EC. *J Eng Mater Tech* 1999;121:189.
- [17] Fleck NA, Hutchinson JW. *J Mech Phys Solids* 1993;41:1825.
- [18] Fleck NA, Hutchinson JW. *Adv Appl Mech* 1997;33:295.
- [19] Gurtin ME. *J Mech Phys Solids* 2000;48:989.
- [20] Gurtin ME. *J Mech Phys Solids* 2002;50:5.
- [21] Bassani JL, Needleman A, Van der Giessen E. *Int J Solids Struct* 2001;38:833.
- [22] Needleman A, Van der Giessen E. *Mater Sci Eng A* 2001;309:1.
- [23] Van der Giessen E, Needleman A. *Modell Simul Mater Sci Eng* 1995;3:689.
- [24] Fleck NA, Ashby MF, Hutchinson JW. *Scripta Mater* 2003;48:179.
- [25] Gao H, Huang Y, Nix WD, et al. *J Mech Phys Solids* 1999;47:1239.
- [26] Huang Y, Gao H, Nix WD, et al. *J Mech Phys Solids* 2000;48:99.
- [27] Stolken JS, Evans AG. *Acta Mater* 1998;46:5109.
- [28] Fleck NA, Muller GM, Ashby MF, et al. *Acta Metall* 1994;42:475.
- [29] Nicola L, Xiang Y, Vlassak JJ, et al. *J Mech Phys Solids* 2006;54:2089.
- [30] Greer JR, Oliver WC, Nix WD. *Acta Mater* 2005;53:1821.
- [31] Yefimov S, Groma I, van der Giessen E. *J Mech Phys Solids* 2004;52:279.
- [32] Xiang Y, Vlassak JJ. *Scripta Mater* 2005;53:177.
- [33] Vlassak JJ, Nix WD. *J Mater Res*. 1992;7:3242.
- [34] Xiang Y, Chen X, Vlassak JJ. *J Mater Res* 2005;20:2360.
- [35] Xiang Y, Tsui TY, Vlassak JJ. *J Mater Res* 2006;21:1607.
- [36] Lu L, Shen YF, Chen XH, et al. *Science* 2004;304:422.
- [37] Christian JW, Mahajan S. *Prog Mater Sci* 1995;39:1.
- [38] Begley MR, Hutchinson JW. *J Mech Phys Solids* 1998;46:2049.